Accelerated keto-enol tautomerization kinetics of malonic acid in aqueous droplets

*Pyeongeun Kim and Robert E. Continetti**

Department of Chemistry and Biochemistry, University of California San Diego, 9500 Gilman Drive, La Jolla, California 92093-0340, USA.

Keywords: organic aerosol, electrodynamic balance, Raman spectroscopy, malonic acid, kinetics, tautomerization

Abstract

Chemical reactions in atmospheric organic aerosol (OA) add large uncertainties to accurate predictions of the effect of aerosol on the health, visibility, and climate. The acceleration of reaction rates of organic compounds in droplets compared to bulk solution has been reported, however, the mechanism and the principle of acceleration largely remains unknown. Malonic acid (MA) is a dicarboxylic acid that exhibits keto-enol tautomerization and is ubiquitous in organic aerosols found in the nature. An environment controlled electrodynamic balance (EDB) coupled with Mie scattering imaging (MSI) and Raman spectroscopy was used to levitate single charged MA droplet and investigate the effect of relative humidity (RH: 90%, 70%, 50%, and 30%) and size (28 – 91 μm diameter) on the reaction kinetics of keto-enol tautomerization of MA. Raman spectroscopy of hydrogen-deuterium isotopic exchange in MA droplets enabled quantitative analysis of MA tautomerization kinetics. The result showed slower reaction rates of MA droplets at lower RH as well as in larger-sized droplets. Application of a step-by-step isotopic exchange model to the MA droplets at 90% RH condition was used to determine the enolization rate of MA, yielding a value 10-fold higher than determined in bulk solution. Keto and enol forms of MA have distinctive physicochemical properties, such as reactivity and hydrogen bond structure. The result from our work suggests that keto-enol tautomerization can play an important role

for aging of MA-containing OA in nature as the enol form of MA can undergo accelerated chemical reactions due to the presence of the reactive carbon-carbon double bond.

Introduction

Organic aerosol (OA) particles constitute a major fraction (20 – 90%) of the submicron particulate mass in the troposphere, and their impact on climate and human health has been recognized for several decades.[1–3] When OA is directly emitted from a source, it is known as primary OA (POA). On the other hand, secondary OA (SOA) can be formed through the oxidation of volatile organic compounds (VOCs) from various biogenic and anthropogenic sources. 'Aging' of POA and SOA occurs through reaction with hydroxyl radicals (OH) or other oxidants present in the atmosphere. Various efforts, from field observations to global atmospheric modeling, have been made to study the reactions in OA and its impact.[4–6] However, aged OA contains a myriad of chemical compounds and this complexity adds significant uncertainty for understanding the physicochemical properties of OA.[7–10] In this regard, it is of particular interest that organic reactions in the droplet phase have been reported to be accelerated compared to the reaction rate in bulk solutions.[11–14] Suggested reasons for this acceleration of reaction rates include partial solvation, entropy effects, concentration effects, and/or fast diffusion.[15] In spite of recent efforts, much remains to be learned about accelerated chemical kinetics in droplets. In this work we will examine this effect in the keto-enol tautomerization of malonic acid as studied by hydrogen/deuterium (H/D) isotopic exchange.

Malonic acid (propanedioic acid, $CH_2(COOH)_2$, MA) is the second acid in the series of aliphatic dicarboxylic acids, after oxalic acid, and it is widely found in atmospheric OA over oceans and urban areas.[16] One characteristic reaction of MA is keto-enol tautomerization (Scheme 1). In dilute aqueous solution states, the keto form of MA dominates over the enol form as the equilibrium constant (K_{eq}) for this reaction has been estimated to be ~10^{-4}.[17] However, a near-edge X-ray fine structure spectroscopy

study of deliquesced MA particles by Ghorai *et al.* showed evidence for a large shift of K_{eq} up to ~2.2 at 90% relative humidity (RH).[18] This observation was supported by the theoretical study of Yamabe *et al.* that suggested possible reaction pathways for keto-enol tautomerization of MA with lower activation energy.[19] They found that a system of six water molecules acts as a catalytic proton relay by forming a hydrogen-bond network with the MA molecule.[19] Although the keto-enol tautomerization of MA in droplets has been studied in terms of keto-enol equilibrium and activation energy,[18,19] no measurements of the chemical kinetics have been reported. Thus, the motivation of this work is to study the reaction kinetics of keto-enol tautomerization of MA and determine how the environmental conditions such as RH and droplet size affect the reaction rates.

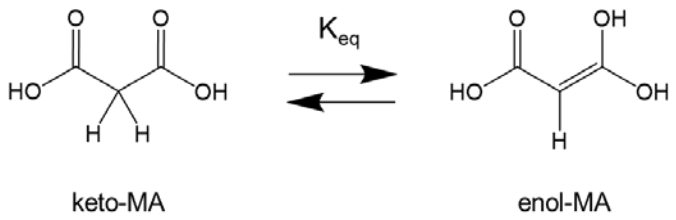

Scheme 1. Keto-enol tautomerization of malonic acid (MA).

To investigate the reaction kinetics of MA in aqueous droplets, an environment-controlled electrodynamic balance (EDB) equipped with Mie scattering imaging (MSI) and a Raman spectrometer has been used. The EDB enables contactless levitation of a single charged droplet at chosen relative humidity (RH) conditions while MSI and Raman spectroscopy provide information about the size, phase, and chemical composition, as well as molecular interactions. One of the frequently used methods for studying reactions in droplets is electrospray ionization mass spectrometry (ESI-MS). Accelerated reactions of various organics in droplets using ESI-MS technique have been reported.[13,20] However, recent study by Rovelli *et al*. asserted limitations of ESI-MS in quantitatively determining acceleration

factors in droplets.[21] The limitations include competition of droplet versus gas phase chemistry and differences in ionization efficiency of analytes.[21] Unlike ESI-MS, the EDB coupled with MSI and Raman spectroscopy allows in-situ investigation of reaction kinetics in a single droplet of constant concentration, in a non-destructive way. Although the EDB setup of this study is incapable of identifying each species involved in the reactions, applying a kinetic model derived from the keto-enol tautomerization mechanism of MA enabled quantitative analysis of reaction rates in levitated MA droplets.

Reaction kinetics of keto-enol tautomerization of MA in aqueous solution can be monitored by using H/D isotopic exchange.[22] In the presence of D_2O as a solvent, H atoms in the carboxylic acid functional groups of MA are rapidly exchanged to deuterium.[22] On the other hand, the α hydrogen atoms attached to the center carbon of MA undergo slower isotopic exchange compared to the acidic hydrogens. This exchange of α hydrogen is mediated by the keto-enol tautomerization mechanism as shown in Scheme 2. During enolization, an α hydrogen of keto-MA is eliminated, resulting in a carbon-carbon double bond. When keto-MA is formed from enol-MA, addition of deuterium to the α carbon takes place in a deuterated environment. Eventually, the α hydrogens of MA are completely exchanged to deuterium through the 4-step mechanism involving 5 MA species (keto_H_2, enol_H, keto_HD, enol_D, keto_D_2) shown in Scheme 2.

In this study, the environment controlled EDB coupled with MSI and Raman spectroscopy was used to investigate the reaction kinetics of keto-enol tautomerization of MA in aqueous droplets of 28 – 91 μm diameter at RH conditions ranging from 90% to 30%. Hydrogen-deuterium isotopic exchange at the α carbon of MA provided a spectroscopic measure of the reaction progress, as the change of C-H stretch (ν(C-H), ~2950 cm^{-1}) and C-D stretch (ν(C-D), ~2200 cm^{-1}) peaks can be readily analyzed. At 90% RH, an explicit step-by-step mechanism was applied to the data to obtain the enolization rate (k_1) of MA. We discovered the enolization was accelerated by up to 10-fold in MA droplets at 90% RH compared to the

literature value from a bulk solution study.[22] At lower RH, viscosity increases and diffusion becomes a dominant contribution to the overall rate, and the detailed mechanism is no longer relevant. To account for this in a simplified quantitative analysis of the RH and size effect on the tautomerization rates, a pseudo-first order approximation was applied. Pseudo-first order approximations are widely used in a range of chemical kinetics studies such as adsorption of dye molecules, hydrolysis of fluorescein diacetate, and dehydration of secondary alcohols.[23–25] Using this approximation, it was observed that the lower RH conditions and larger droplet size reduce the tautomerization rate of MA. The size effect becomes more evident for droplets at lower RH conditions. In the following section the experimental method will be presented in detail.

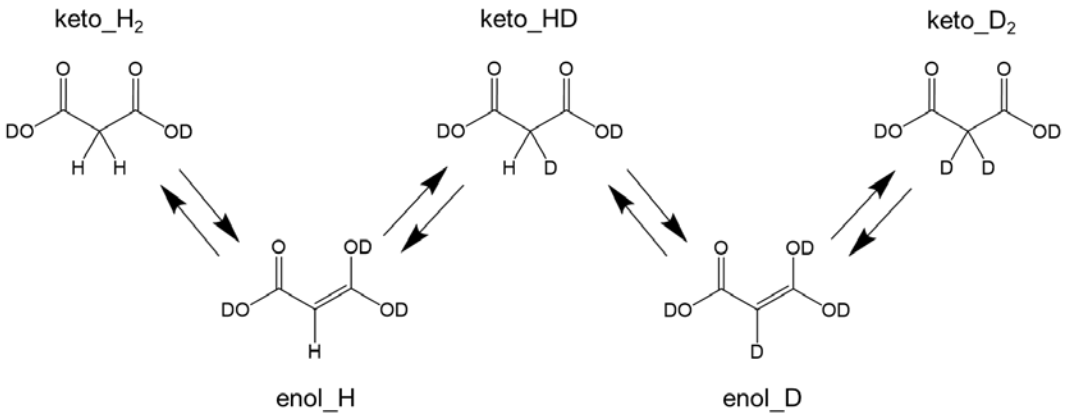

Scheme 2. Propagation of hydrogen-deuterium exchange (C-H to C-D) of MA through keto-enol tautomerization.

Experimental Methods

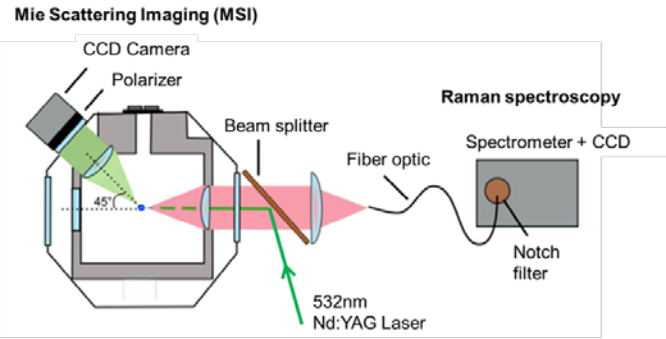

Figure 1. Schematic diagram of the electrodynamic balance (EDB) with Mie scattering imaging (MSI) and Raman spectroscopy. A single MA droplet trapped inside the chamber is being illuminated by a pulsed 532nm laser. The MSI pattern (green shade) is captured from the camera located at the 45° forward direction of scattering whereas backscattered Raman signal (red shade) is collected through the fiber optic coupled with spectrometer and CCD detector.

Details of the environment-controlled EDB coupled with Mie and Raman spectroscopy have been described in previous work from this laboratory.[26,27] The reagents, Malonic acid (99%, Aldrich) and D_2O (99.9% D, Cambridge Isotope Laboratories) were used as purchased without further purification. MA was dissolved in HPLC-grade water (max. 1 ppm residue after evaporation, Fisher Chemical) with concentrations of 3 molal and 6 molal. 3 molal solutions generate relatively smaller size droplets compared to 6 molal solutions, because the size of the droplet is determined by the amount of solute present in each droplet at a given RH condition. The MA solutions were loaded into a piezoelectric droplet generator (Engineering Arts DE03) using a motorized syringe. The MA solution was then introduced as a burst of 30 droplets into the environmental chamber equilibrated at the desired RH of D_2O. The RH inside the chamber was controlled by a constant flow of dry and humid N_2 gas into the chamber, with the humidity controlled by bubbling N_2 through a D_2O bubbler held at room temperature.

The flow rates of the gases were controlled by digital mass flow controllers (Alicat MC-500SCCM) with a total flow rate of 120 sccm (cm^3/min). The burst of droplets was generated by a user-selected waveform that drives the piezoelectric element to induce tip vibration and eject the loaded solution. Droplet charging was controlled using the grounded metallic tip of the droplet generator in a circuit with an inductive charging ring to induce an imbalance of charge as the droplets were generated, yielding charged droplets (<40 elementary charges per μm^2).[26] A radio frequency (RF) sine wave generated from a frequency synthesizer (Agilent 33210A) was amplified by a set of amplifiers (Krohn-Hite 7602M wideband amplifier and Matsusada AMS 1.5kV high voltage amplifier) and directed to two conical-shaped endcap electrodes of the trap located at the center of the chamber. The combination of RF voltage from the endcap electrodes and a DC potential (Stanford Research Systems PS350) applied to two rod electrodes at the bottom of the trap were adjusted until a single droplet was confined and stabilized at the null point of the alternating electric field.[28] Typical trapping conditions for MA droplets were 90 - 180Hz, 1.5kV (rms) AC and 200 - 400V DC depending on droplet size (mass).

The schematic layout of MSI and Raman spectroscopy setup is shown in **Figure 1**. The levitated MA droplet was illuminated by a vertically polarized pulsed 532nm Nd:YAG laser (RMPC Wedge XF, 500 – 700ps pulse width, 1 – 40kHz repetition rate) with 25-50mW average power. The perpendicular-polarized Mie scattering pattern was collected in the 45° forward direction with respect to the laser path using a charge-coupled device (CCD) camera equipped with a polarizer. Collected Mie scattering images were processed using a MATLAB script to obtain the diameter of MA droplets in the geometrical optics approximation.[29,30] The refractive index of MA droplets at all RH conditions were calculated using parameters adopted from the study by Cai *et al* (**Figure S5** in the Supplementary Information (SI)).[31] The droplet size calculated using MSI ranged between 28 – 91 μm in diameter (±0.5 μm error due to the uncertainty of RH). The Mie scattering images of MA droplets showed regular fringes of diffraction

patterns under all RH conditions (**Figure S2**), indicating that no phase-transitions occurred under the conditions of these measurements.

The Stokes-shifted Raman signal of all polarization was collected using a fiber optic located in the backscattering direction (180°) of the laser path into the chamber. The fiber optic introduced the Raman signal into the spectrometer (Acton SpectraPro 275, f/3.8) equipped with a 600 g/mm grating. The spectral image obtained by the thermoelectric-cooled CCD detector (Horiba Syncerity) was converted into the Raman spectra presented here. Raman measurements were made after stable levitation of the droplet in the EDB was achieved. Typical time difference between introduction of the droplet into the chamber and measurement of the first Raman spectrum (t = 0 s) was ~2 minutes. The integration time varied between 30 and 120 seconds depending on the size of the droplets. Generally, smaller droplets needed longer exposure for better signal to noise ratio (S/N).

Measurements were made at D_2O RH conditions of 90%, 70%, 50%, and 30% (±1.5%) and ambient temperature (19–21 °C). The temperature and RH of the chamber was determined using a capacitive sensor (Vaisala Humicap 180R). The humidity data measured by the sensor were converted according to the difference in equilibrium vapor pressure of D_2O versus H_2O.[32]

Analysis of the spectra was supported by density-functional theory calculations of the Raman signals using Gaussian 09 software. The level of theory used to calculate the Raman shift and Raman activities for the optimized structures of MA molecules with every conformation in Scheme 2 was B3LYP/6-311++g(d,p). All other data processing was carried out using MATLAB.

Results

In the following section, dynamic Raman spectra of an MA droplet in the 1500 – 4000 cm^{-1} spectral region will be presented. The dynamic spectra will be used to describe reaction kinetics of keto-enol tautomerization of MA by observing evolution of the ν(C-H) and ν(C-D) peaks as changes in these peaks are caused by H/D exchange during the tautomerization. The effect of size and RH on the H/D exchange and tautomerization rates will then be presented.

The C-H/C-D exchange of malonic acid droplets revealed by dynamic Raman spectra

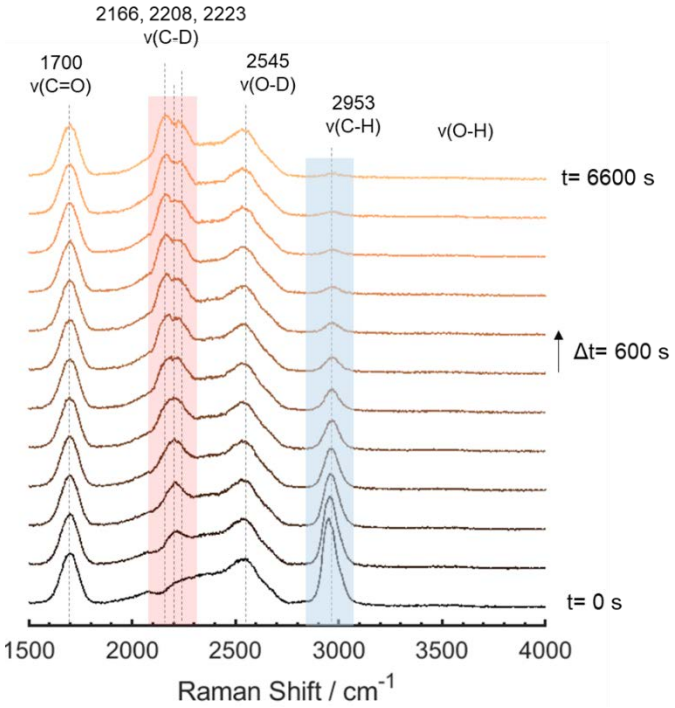

Figure 2. Dynamic Raman spectra of a MA droplet of 57.3 µm diameter undergoing H/D exchange at 50% RH. Timestep between each spectrum is 10 minutes (600 seconds). The rise of intensity of the ν(C-D) peaks (2166, 2208, 2223 cm^{-1}) is highlighted with a red shade while the intensity decrease of the ν(C-H) peak (2950 cm^{-1}) is emphasized with a blue shade. All spectra are normalized to the intensity of ν(C=O) peak (1700 cm^{-1}).

Time-resolved Raman spectra of MA droplets levitated in the EDB and equilibrated under the desired D_2O-RH conditions evolve in a manner consistent with C-H/C-D exchange kinetics. The rate of exchange was found to be affected by the RH in the EDB chamber and size of the droplet, and the time-resolved Raman spectra allow a quantitative analysis of the kinetics of isotopic exchange. **Figure 2** shows dynamic spectra of a MA droplet (57 μm diameter) undergoing C-H/C-D exchange at 50% RH. The decrease in intensity of the v(C-H) peak at ~2935 cm^{-1} and the rise of v(C-D) peaks at ~2166 and ~2223 cm^{-1} indicate the equilibrium of MA droplet shifts from keto_H_2 ⇌ enol_H to keto_D_2 ⇌ enol_D over the timescale of 1 – 2 hours. The RH and size dependencies of the rate of isotopic exchange will be discussed in later section.

Table 1. Calculated values of Raman shift and Raman activity of C-D and C-H stretch vibration.

Species	v(C-D)		v(C-H)	
	Raman Shift (cm^{-1})	Raman Activity ($Å^4$/amu)	Raman Shift (cm^{-1})	Raman Activity ($Å^4$/amu)
keto_H_2	-	-	3123 (asym) 3073 (sym)	48 (asym) 106 (sym)
Enol_H	-	-	3232	61
Keto_HD	2268	42	3107	71
Enol_D	2387	26	-	-
Keto_D_2	2315 (asym) 2236 (sym)	25 (asym) 52 (sym)	-	-

In the dynamic Raman spectra recorded as a function of time in **Figure 2**, some spectroscopic features reveal valuable details of the C-H/C-D exchange process. First, it is worth noting that at the beginning of the experiment (t = 0 s), there was already no observable v(O-H) band present at 3000 – 3800 cm^{-1} region. Conversely, the v(O-D) band at 2000 – 2700 cm^{-1} exists from t = 0 s and the band does

not show major intensity changes over the course of the experiment. The Raman ν(O-H) band would have two intensity contributions – from water (H-O-H) and the carboxylic acid functional groups (-COOH) from MA. Therefore, the analysis of the ν(O-H) and ν(O-D) bands supports our assumption that the MA droplets establish rapid equilibrium with the D_2O-environment upon the initial droplet generation and levitation, and -COOH/-COOD isotopic exchange is much more rapid than C-H/C-D exchange. Second, the splitting of the ν(C-D) peak is observed as the exchange continues. The ν(C-D) peak near 2208 cm^{-1} emerges at the beginning (t = 600 – 1800 s) of the exchange and eventually splits in to two peaks at near 2166 and 2223 cm^{-1} towards the end point of the exchange (t = 3600 – 6600 s). This splitting of the ν(C-D) peak can be explained by evaluating vibrational frequencies of molecules involved in the exchange process, in particular, for the C-D stretch vibrations of the keto_HD, keto_D_2, and enol_D molecules. **Table 1** lists the calculated frequencies and Raman activities for the C-H and C-D stretch vibrations. During the course of isotopic exchange, the equilibrium shifts from keto_H_2 ⇌ enol_H to keto_D_2 ⇌ enol_D with keto_HD as an intermediate. From **Table 1**, it can be noticed that the ν(C-D) frequency of keto_HD (2268 cm^{-1}) lies between those of keto_D_2 (sym. 2236 and asym. 2315 cm^{-1}) and enol_D (2387 cm^{-1}). Accordingly, assessing the calculated vibrational frequencies listed in **Table 1**, three ν(C-D) peaks (2166, 2208, 2223 cm^{-1}) found in **Figure 2** can be assigned as keto_D_2, keto_HD, and enol_D of MA, respectively. The symmetric and asymmetric ν(C-D) frequencies are not distinguishable in these spectra possibly due to the smaller Raman intensity of the asymmetric ν(C-D) compared to the symmetric ν(C-D) and the overlap between other ν(C-D) peaks.[33] Lastly, the intensity of the ν(C=O) peak at 1700 cm^{-1} does not noticeably change during the progression of isotopic exchange. Thus, the dynamic spectra of **Figure 2.** are normalized using the Raman intensity of ν(C=O) peak. This near-steady intensity of the ν(C=O) peak indicates the keto:enol ratio of MA stays constant during the isotopic exchange of a MA droplet. The intensity of the ν(C=O) peak would fluctuate if the keto:enol ratio changed over time as keto-MA contains two carbonyl groups (C=O) while enol-MA has one C=O.[18]

Size and RH dependency of H/D exchange and keto-enol tautomerization kinetics.

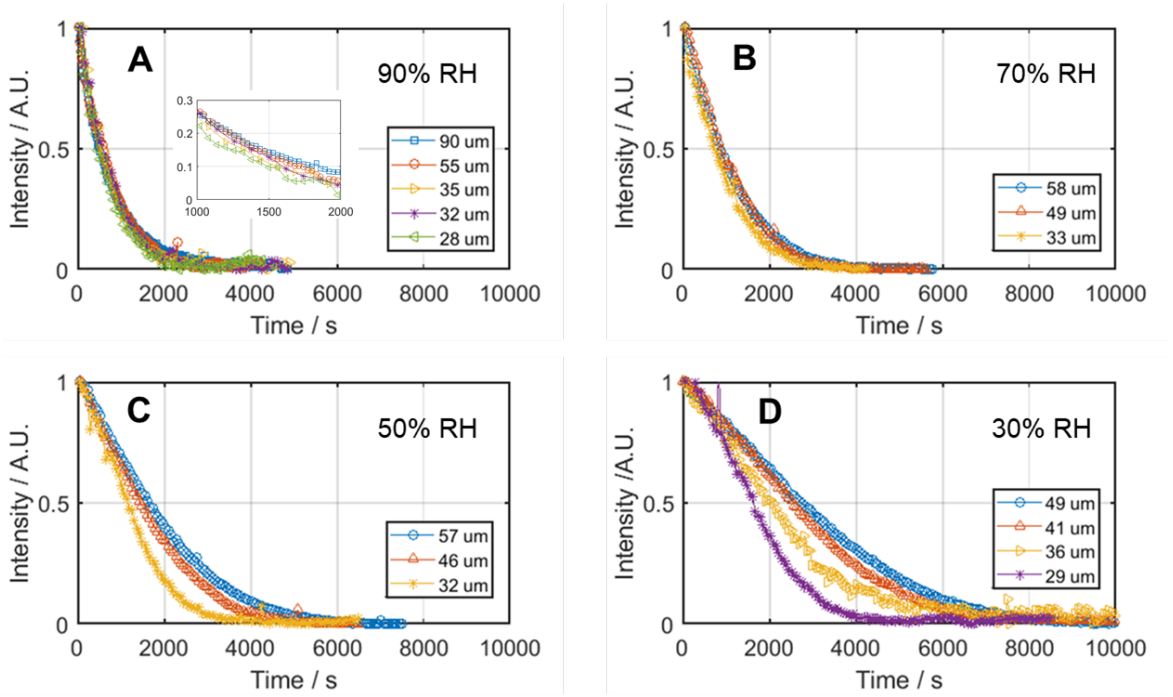

Figure 3. Integrated Raman intensity of ν(C-H) peak of MA droplets (28 – 91 µm diameter) as a function of time at 90% (A), 70% (B), 50% (C), and 30% RH (D). The inset of (A) is a magnified plot at 1000 – 2000 s timeframe to show the difference in intensities of various-sized droplets. Size dependency of isotopic exchange rates is more pronounced in lower RH conditions.

The rate of C-H/C-D exchange is affected by both RH and size of the droplet. **Figure 3** shows the ν(C-H) Raman intensity versus time at 90%, 70%, 50%, 30% RH for various sizes of the MA droplets (28 – 91 µm diameter). It has been observed that the size of MA droplet plays a more important role in isotopic exchange rates at lower RH conditions. **Figure 3A** shows that at 90% RH, droplet size has a minimal effect on the exchange kinetics. As the condition gets drier (**Figure 3B, C, and D**), a general trend is observed that the exchange rates are relatively slower for larger MA droplets. The impact of RH on the exchange kinetics can be clearly noticed in **Figure 4**. **Figure 4A** shows the data for droplets in the size

range of 45 – 55 µm diameter while **Figure 4B** shows the data for droplets of 31 – 33 µm diameter. For both size groups of MA droplets, it is observed that the rate of isotopic exchange is faster for droplets at higher RH.

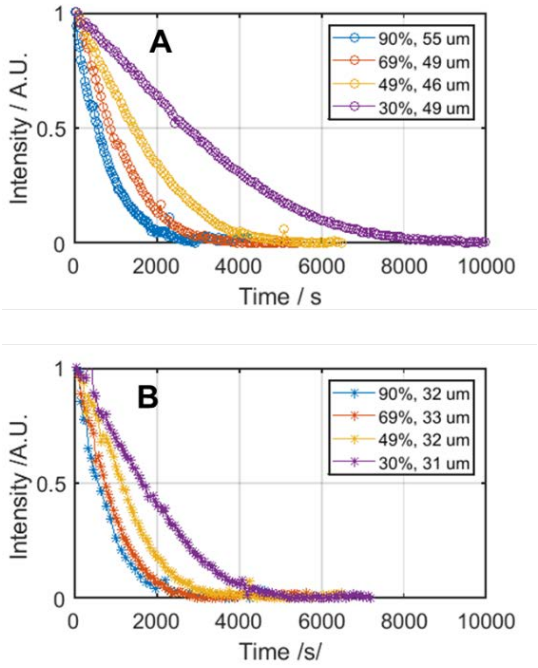

Figure 4. Integrated Raman intensity decrease of ν(C-H) peak over time for two different size ranges of MA droplets, 46 – 55 µm diameter (A) and 31-33 µm diameter (B). Smaller droplets show a faster overall rate of isotopic exchange than larger droplets. Additionally, there is larger influence of RH conditions on the larger droplets compared to smaller droplets.

Discussion

In this section, the quantitative analysis of the reaction kinetics will be carried out by applying q pseudo-first order approximation to the experimental data. For MA droplets at 90% RH, step-by-step kinetic model for isotopic exchange will then be used to estimate the enolization rate coefficient (k_1) of MA. In

addition, broader implications of the result of this study to the current understanding of atmospheric OA particles and their complex chemistry will be discussed.

Application of pseudo-first order to the isotopic exchange kinetics

For quantitative analysis of the isotopic exchange kinetics of MA droplets of various sizes and under varying RH conditions, a pseudo-first order approximation method is applied for the ν(C-H) Raman intensity versus time data. In this study, the premise for this approximation is that the entire system of isotopic exchange (**Scheme 2**) can be simplified to the reaction that only involves C-H and C-D functional groups. This simplified exchange reaction is schematically illustrated in **Scheme 3**. The hydrogen atom that is covalently bonded to the α carbon of MA undergoes the reversible isotopic exchange reaction with a D_2O molecule, thus producing C-D and HOD. The rate coefficients for the forward (C-H to C-D) and reverse (C-D to C-H) are noted as k_f and k_r, respectively. In addition, HOD/D_2O exchange at the droplet surface is considered as the droplet is in dynamic equilibrium with the vapor phase of D_2O with a set RH condition. The HOD/D_2O exchange coefficient is given as k_{ex}, thus the overall gas-droplet exchange rate at the surface is related to surface to volume ratio (S/V) and k_{ex}.

In this simplified picture of H/D exchange of MA, there are two possible scenarios for higher RH conditions and lower RH conditions. At higher RH conditions where diffusion rate and gas-droplet exchange are fast, reverse H/D exchange can be ignored due to the rapid extinction of HOD in the droplet. Therefore, in scenario A, observed rate coefficient (k_{obs}) is only dependent on the forward (k_f) H to D exchange (Scheme 3). In this case where $[HOD]$ is negligible, the pseudo-first order rate of disappearance of ν(C-H) Raman intensity over time can be interpreted by defining k_{obs} from the experimental data. **Figure 5** shows examples of the application of the pseudo-first order approximation

to the experimental data for droplets at 90% RH and 50% RH. In **Figure 5**, the data were fit with the following equation (eq. 1),

$$I_{obs}(t) = I_0 e^{-k_{obs}t} \quad (1)$$

where $I_{obs}(t)$ is the integrated intensity of ν(C-H) peak intensity, I_0 is the initial integrated intensity of ν(C-H) peak, k_{obs} (observable rate coefficient) is the fitting parameter, and t is time in seconds.

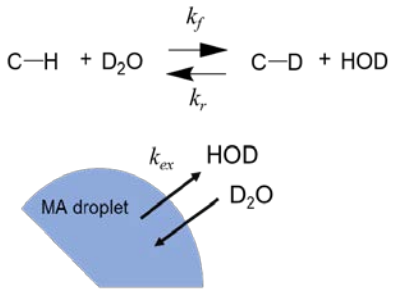

Scenario 1 (High RH) : $k_{obs} = k_f[D_2O]$

Scenario 2 (Low RH): $k_{obs} = k_f[D_2O] - k_r[HOD]$

Scheme 3. Description of forward (k_f) and reverse (k_r) reaction of isotopic exchange as well as gas-droplet exchange interaction (k_{ex}) at the surface. Two scenarios for the pseudo-first order approximation can be considered depending on the rate of the reverse exchange reaction determined by $k_r[\mathrm{HOD}]$.

For a 35 μm droplet at 90% RH (**Figure 5A**), $I_{obs}(t)$ displays excellent agreement with the experimental data, suggesting the isotopic exchange kinetics under these conditions can be suitably approximated to the first order reaction. At 50% RH (**Figure 5B**), however, there exists a deviation of first-order exponential $I_{obs}(t)$ from experiment, where the earlier stage of the data (≤ 1500 s) shows a linear decrease in intensity rather than exponential decay. To understand this divergence from the pseudo-first order approximation in the data, a second scenario where $[HOD]$ cannot be ignored must be considered. As seen in Scheme 3, C-D and HOD can undergo reverse exchange reaction and $[HOD]$ is

highly dependent on S/V of the droplet, k_{ex}, and overall diffusion rate in the droplet. Therefore, the value of k_{obs} is the result of competing of forward and backward H/D exchange reactions as well as the gas-droplet exchange at the surface. These perturbations are not the only source of deviation of the fit from the pseudo-first order (**Figure 5B**) - the size and RH dependency of k_{obs} can also be explained in terms of k_r and k_{ex}. Applications of the pseudo first-order approximation to MA droplets at all experimental conditions are shown in the SI in **Figure S3**.

The observable rate coefficients (k_{obs}) are obtained under the various experimental conditions and are listed in **Table 2**. It should be noted that applications of the pseudo first-order approximation diverge more from the experimental data for lower RH and bigger droplets. Therefore, this discrepancy reflects the effect of k_r and k_{ex}. However, the pseudo-first order approximation with its fitting parameter k_{obs} provides a quantitative measure for overall C-H/C-D exchange rate and enables further analysis of kinetics for varying experimental conditions. The values of k_{obs} under the full experimental conditions are presented in **Figure 6**. It is apparent from the **Figure 6** that the isotopic exchange rate is slower at relatively lower RH conditions. This deceleration of the kinetics at lower RH is due to the increasing viscosity which leads to the slow diffusion of the molecules in the droplet following exchange at the gas-droplet interface.[34,35] Higher viscosity at lower RH results in a slower diffusion rate and exchange rate (k_{ex}), leading to the accumulation of HOD, which eventually promotes reverse reaction (k_r) of Scheme 3 and lowers k_{obs}. Along with the effect of RH on k_{obs}, a larger droplet size also leads to slower isotopic exchange kinetics. Bigger droplets have lower surface to volume (S/V) ratios, limiting surface HOD-D_2O exchange for the increased HOD production that is proportional to the volume of the droplet. In addition, in bigger droplets, it takes longer for HOD molecules to diffuse to the surface for the HOD-D_2O exchange. Therefore, larger droplet sizes lower the value of k_{ex}, eventually causing slower isotopic exchange (lower k_{obs}) for conditions of RH 70% and below. Surprisingly, the size of the droplet has only minor impact on the isotopic exchange kinetics at 90% RH condition. Along with the fact that at

90% RH the experimental data for ν(C-H) intensity decrease over time showing a near first-order exponential decay, it can be argued that the diffusion rate of HOD and the gas-droplet interaction are fast enough to ignore the reverse reaction of Scheme 3. In other words, C-H/C-D exchange kinetics of MA droplets at 90% RH can be successfully approximated to the first-order reaction with a slight size effect.

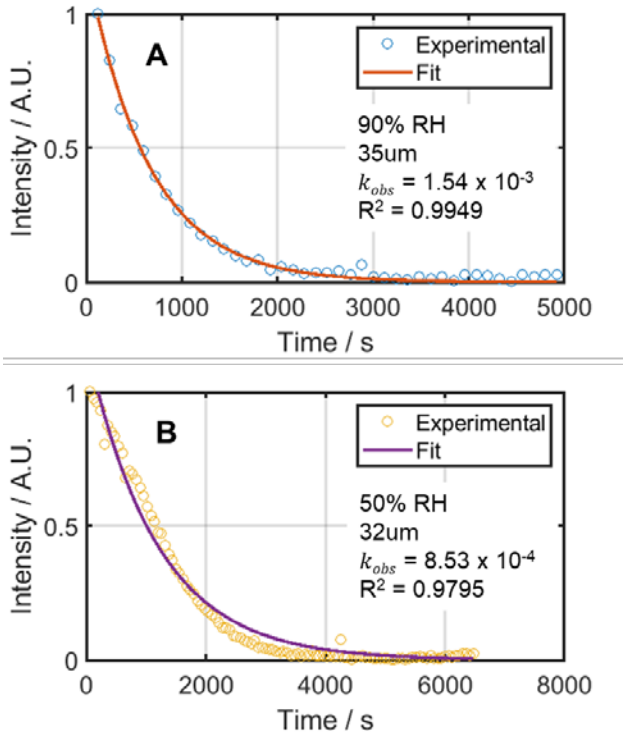

Figure 5. Result of least-squares fit of pseudo-first order approximation (eq. 1) to the experimental data of ν(C-H) intensity over time for 35μm diameter droplet at 90% RH (A) and 32μm diameter droplet at 50% RH (B). Open circles represent experimental data and solid line curves are pseudo-first order fit. The MA droplet at 90% RH (A) show better agreement of the data to the pseudo first-order approximation compared to the droplet at 50% RH (B).

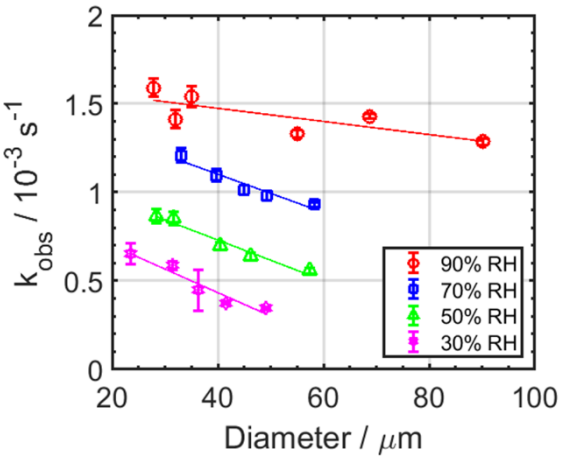

Figure 6. Values of observable rate coefficient (k_{obs}) for all MA droplets plotted with droplet diameter and RH condition. Error bars represent 95% confidence interval of the fit (eq. 1 to the ν(C-H) intensity).

Table 2. Values of k_{obs} derived from pseudo-first order approximation for all MA droplets.

RH (%)	d (μm)	$k_{obs}/10^{-3}$ (s^{-1})	RH (%)	d (μm)	$k_{obs}/10^{-3}$ (s^{-1})
90	90.5	1.29 ± 0.02	50	57.3	0.56 ± 0.02
	68.8	1.43 ± 0.02		46.2	0.64 ± 0.02
	55.0	1.33 ± 0.02		40.4	0.70 ± 0.02
	35.1	1.54 ± 0.06		31.7	0.85 ± 0.04
	32.0	1.54 ± 0.06		28.4	0.86 ± 0.04
	27.8	1.59 ± 0.05	30	49.1	0.34 ± 0.01
70	58.2	0.93 ± 0.01		41.5	0.38 ± 0.01
	49.3	0.98 ± 0.03		36.3	0.45 ± 0.1
	45.0	1.02 ± 0.03		31.4	0.59 ± 0.02
	39.7	1.10 ± 0.03		23.5	0.65 ± 0.06
	33.0	1.21 ± 0.04			

Estimation of rate coefficient (k_1) for enolization of MA using step-by-step kinetic model

As discussed in the previous section, the isotopic exchange kinetics of MA droplets at 90% RH are the least size-dependent under the experimental conditions in this study, thus the reverse reaction involving HOD can be ignored due to fast diffusion and gas-droplet exchange. This assumption for MA droplets at 90% RH allows a step-by-step description of the isotopic exchange process as given in Scheme 4. It should be noted that Scheme 4 is a step-by-step representation of Scheme 2, with reactions involving HOD neglected under the assumption that as an intermediate in the deuterated environment it will not accumulate appreciably. Rate coefficients for keto to enol (enolization) and enol to keto (ketonization) are indicated as k_1 and k_2, respectively. k_1' and k_2' are the corresponding rate coefficients with the secondary kinetic isotope effect (KIE). The value for KIE=1.3 has been adopted from the ^{1}H NMR study of malonic acid isotopic exchange by Hansen *et al*.[22] To establish a mathematical model and to derive kinetic parameters from the data using the model, a minimum number of unknown variables is necessary. The X-ray absorption fine structure study of deliquesced MA particles by Ghorai *et al.* determined the value of the equilibrium constant (K) for keto-enol tautomerization of MA droplet to be 2.2 ± 0.4 at 90% RH,[18] and we have used that value to minimize the unknown variables in the step-by-step model.

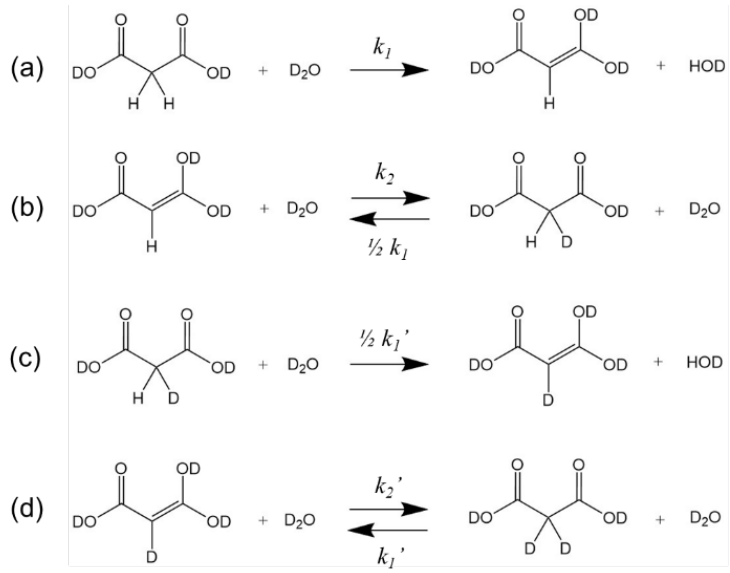

$k_1' = k_1/KIE$ $\quad KIE = 1.3$ $\quad K = k_1/k_2 = 2.2$

$k_2' = k_2/KIE$

Scheme 4. Step-by-step kinetic model derived from C-H/C-D exchange mechanism of MA. k_1 and k_2 are rate coefficient for enolization and ketonization, respectively.

A series of ordinary differential equations (ODEs) describing the step-by-step kinetic model given in Scheme 4 can be simply represented in matrix notation (**SI Note 1**). This mathematical modeling is a standard method for quantitative analysis of H/D isotopic exchange reactions.[20] Solving this series of ODEs with the aid of the relationships of kinetic parameters discussed above (Scheme 4) yields the concentration of each compound as a function of time, as shown for the five species in **Figure 7**. It is noticeable from **Figure 7** that concentrations of initial compounds (keto_H_2 and enol_H) decrease over time and those of deuterated compounds (keto_D_2 and enol_D) rise while the concentration of intermediate keto_HD increases at first then decays, as expected for an intermediate in a multistep reaction sequence. This evolution of each specie from solving model ODEs can explain the splitting of ν(C-D) peak shown in **Figure 2**. The dynamic series of spectra in **Figure 2** show that the ν(C-D) peak

initially emerges near 2208 cm-1, then splits into two peaks around 2166 and 2223 cm^{-1}. Referring to the DFT calculations (**Table 1**), the Raman shift of the intermediate keto_HD (2268 cm^{-1}) lies between keto_D_2 (2236 cm^{-1}, symmetric) and enol_D (2387 cm^{-1}). Therefore, it can be suggested that initial increase of ν(C-D) peak at ~2208 cm^{-1} is caused by formation of intermediate keto_HD and the splitting of ν(C-D) peak is due to the conversion of keto_HD into of fully deuterated species (keto_D_2 and enol_D).

The solutions of the system of ODEs can be combined to simulate the experimental data given in **Figure 3A**. To represent the ν(C-H) intensity decrease, the solutions of $keto\_H_2(t)$, $enol\_H(t)$, and $keto\_HD(t)$ need to be summed with appropriate coefficients. Although the number of C-H oscillators for each element is 2, 1, and 1, respectively, this does not consider the Raman intensities for these oscillators. Accordingly, the calculated Raman activity coefficient for every ν(C-H) and ν(C-D) vibration has been used to simulate the data with the maximum fidelity (**Table 3**). The equations for ν(C-H) and ν(C-D) intensity are given as,

$$I_{CH}(t) = (48 + 106)\, keto\_H_2(t) + 61\, enol\_H(t) + 71\, keto\_HD(t) \quad (2)$$

$$I_{CD}(t) = (25 + 52)\, keto\_D_2(t) + 26\, enol\_D(t) + 42\, keto\_HD(t) \quad (3)$$

where $I_{CH}(t)$ and $I_{CD}(t)$ represent Raman intensity of (C-H) and ν(C-D) peak, respectively, and the integer factors are the relative Raman activities. The values of Raman activity coefficient for all the species are given in **Table 1**.Since the right side of eq. 2 contains solutions of ODEs set up using step-by-step model (**Scheme 4** and **SI Note 1**), $I_{CH}(t)$ is a function of time with an unknown parameter, k_1. Therefore, eq. 2 can be used to fit the simulated Raman intensity ($I_{CH}(t)$) to the time evolution of ν(C-H) peak to estimate the value of enolization rate coefficient k_1. Then, using the obtained value of k_1 from the fit of eq. 2, $I_{CD}(t)$ is constructed from the solutions of ODEs to verify that eq. 3 shows adequate agreement with the data of ν(C-D) intensity increase. The comparison of the simulated $I_{CH}(t)$ and

$I_{CD}(t)$ with the experiment is shown in **Figure 7B**. Verification for the full range of droplet sizes is available in Supplementary Information (**Figure S1**). For MA droplets at RH 90% condition excellent agreement was found between the experimental data and the simulated intensity functions created using the step-by-step model. The values of $[D_2O]k_1$ are listed in **Table 4**. The value of $[D_2O]$ is assumed to be same for every droplet at 90% RH because at the given experimental conditions, RH is the only factor that determines the water content in MA droplets. Similar to the pseudo-first order approximation analysis, small dependency on size is observed, as the difference of the value of k_1 is about 22% for the biggest (90.5 μm) and smallest (27.8μm) MA droplets (**Table 4**). This minor size effect may originate from the elongated diffusion time of HOD to reach the surface for HOD-D_2O exchange in larger droplets as discussed in the previous section.

While there is no previous study on keto-enol tautomerization kinetics of MA in aqueous droplets, Hansen *et al*. reported the enolization rate coefficient ($[D_2O]k_1$) of MA to be 1.066 x 10^{-3} in 1M D_2SO_4 solution.[22] Comparing this value of $[D_2O]k_1$ with the data from this study, our result shows a 10-fold increase in the enolization rate coefficient. It should be noted that the bulk measurement was performed at a MA concentration of 0.25 M while the concentration of MA in a droplet at 90% RH is 3.35 M, thus the comparison is not a direct one.[31] This dramatic acceleration is more striking considering MA droplets only consist of MA and D_2O, without any acidic compound added to facilitate enolization. The pH of 1M D_2SO_4 solution is close to 0, and the pH of MA droplet at 90% RH is expected to be ~ 1 according to Raman spectroscopic study by Chang *et al*.[36] C-H/C-D exchange can be catalyzed by the presence of acid, base, and/or water.[20] It is safe to say that the pH is not responsible for acceleration of enolization rate in MA droplet, because the droplets in this study have higher pH than 1M D_2SO_4. Yamabe *et al.* suggested that the activation energy of keto-enol tautomerization of MA can be significantly lowered by a hydrogen bonded water-MA network.[19] According to their calculation, the transition state was most stabilized when a single MA molecule is surrounded by 6 water molecules as

they form a proton-relay network.[19] Water-catalyzed reaction paths provide another explanation on why isotopic exchange rates are slower at lower RH conditions (**Figure 6**). The water to solute ratio (WSR) of MA droplets at given RH conditions can be modeled using the modified-UNIFAC (Universal quasichemical Functional group Activity Coefficients) parametrization (**Figure S4**).[37,38] 90%, 70%, 50%, 30% RH conditions correspond to the WSR of 10:1, 3:1, 1.5:1, 0.7:1 for MA droplets. The catalytic proton-relay facilitated by the hydrogen bond network (WSR of 6) would thus be more favorable for MA droplets at 90% RH than the drier conditions. Less solute-water interaction is available in droplets at lower RH, leading to slower keto-enol tautomerization rates.

The hydrogen bond network of organic aerosol (OA) is highly affected by the RH, since the WSR and solute-water interaction change with respect to the functional groups of solutes.[27] It should be noted that isotopic exchange kinetics in MA droplets is a complex system difficult to completely unravel because it is intertwined with numerous factors to consider such as reaction, diffusion, and gas-surface interaction. However, our result in **Table 3** shows that the keto-enol tautomerization rate is significantly accelerated (10-fold) in the droplet phase compared to bulk solution, facilitated by the catalytic role of the hydrogen-bonded water-solute network on the enolization reaction of MA. In addition, the value of the estimated enolization coefficient (k_1) versus size of the droplet (**Table 3**) shows a similar trend as discussed earlier (**Figure 6**) in that the reaction rates are faster for smaller droplets. Although the size dependency of tautomerization reaction rates in MA droplets are primarily due to the diffusion effect, the acceleration of reactions at gas-droplet interface may contribute to the overall reaction kinetics.[39] However, surface behavior of MA is outside the scope of this paper and requires further investigation with surface-sensitive techniques such as sum-frequency generation (SFG) spectroscopy.[40–43]

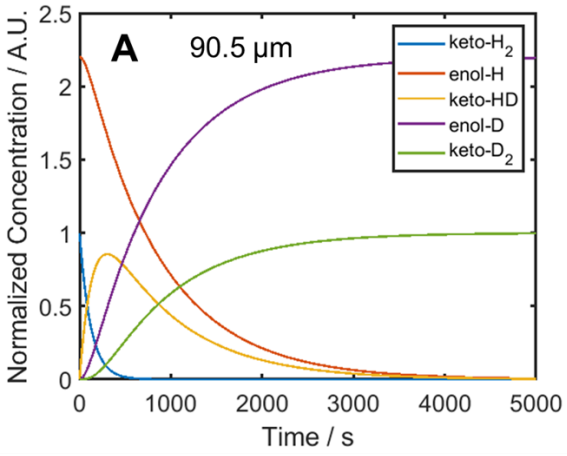

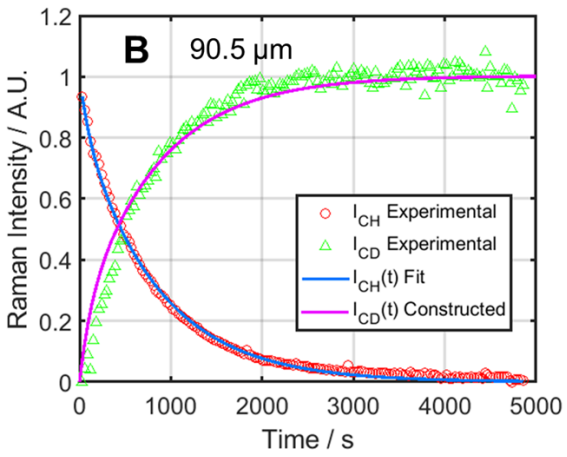

Figure 7. (A) Normalized concentration of all the species in MA droplet (90.5 µm diameter) as a function of time from a solution of the ODEs describing the step-by-step kinetic model (SI Note 1) during isotopic exchange at 90% RH. (B) Application of the kinetic model to the experimental data. Solid blue line shows the least-squares fit of eq. 2 to the experimental data. The solid magenta line represents eq. 3 constructed using the value of k_1 derived from the fitting of eq. 2. Similar plots for MA droplets of all sizes at 90% RH are available in **Figure S1**.

Table 3. Estimated enolization rate coefficients ($[D_2O]k_1$) of MA in aqueous droplets at 90% RH. The value of $[D_2O]k_1$ from the bulk solution study is 1.066 x 10^{-3} s^{-1}.[22] Errors of $[D_2O]k_1$ originate from the error of keto-enol equilibrium constant (K) which value was assumed to be 2.2 ± 0.4.[18]

RH (%)	d (μm)	$[D_2O]k_1/10^{-3}$ (s^{-1})
90	90.5	8.2 ± 1.1
	68.8	8.5 ± 1.1
	55.0	8.2 ± 1.1
	35.1	10.2 ± 1.4
	32.0	8.5 ± 1.2
	27.8	10.2 ± 1.4

Implications for SOA formation and aging of atmospheric OA particles

There are important implications of the results of this study. First, accelerated keto-enol tautomerization kinetics of MA may promote unexpected chemical reactions in atmospheric OA particles. Usually, enols of simple aliphatic compounds have a short lifetime compared with their keto tautomers.[44] However, for MA, the previous experimental[18] and theoretical[19] studies imply that the enol form of MA may exist in larger fractions in aqueous droplets compared to dilute bulk solutions. Furthermore, the work of Lim *et al*. has shown aqueous chemistry in SOA formation including aldol condensation, sulfur esters formation, and oligomerization of hydrated glyoxal enols.[45] Another theoretical study by Lei *et al*. showed atmospherically relevant reactions of ethenol with OH radical, with glycolaldehyde is predicted to be the main product.[46] According to these observations, our results strongly suggest that it may be possible that MA in the atmospheric OA particles can undergo unpredicted chemical reactions with other organic compounds and form low-volatility SOA products in the presence of highly reactive species such as OH radical. Furthermore, the rate of reactions involving MA can be faster than the general assumption for OA aging. This unpredictability of MA reaction kinetics

can have considerable impact on aging of OA because MA is found in significant concentrations in aerosols.[16,47]

Also, the enhanced enolization and unexpected chemical reactions of MA in aqueous droplets can hinder the accurate description of physicochemical properties of OA by thermodynamic models. For the complex system represented by OA, the AIOMFAC (Aerosol Inorganic-Organic Mixtures Functional groups Activity Coefficients) thermodynamic model has been widely used to predict activity coefficients of each compound in OA system.[48] Models based on AIOMFAC need information about the number of organic functional groups present to calculate interactions between functional groups and inorganic ions, then predict physicochemical properties such as gas-particle partitioning and hygroscopic properties of OA.[48,49] However, the fact that MA can exist in dynamic equilibrium of keto form (2 -COOH and 2 C-H groups) and enol form (1 -COOH, 1 C-H, and 2 -OH groups) adds uncertainty to the precise prediction of physicochemical properties of MA-containing OA. Field observation studies by Kawamura *et al.* have shown that MA is the second most abundant dicarboxylic acid in marine aerosols.[16] In addition, the variability of functional groups due to keto-enol tautomerization of MA can affect the overall hydrogen bond network in OA. The impact of hydrophilic functional groups (-OH and -COOH) on the hydrogen bond network of OA has been reported in our previous work.[27] Changes in the hydrogen bond network of MA-water system due to the contribution from different functional groups may affect the macroscopic physicochemical properties of OA particles, i.e., viscosity, water diffusion, and hygroscopic properties.

Conclusion

The reaction kinetics of keto-enol tautomerization of aqueous MA droplets were studied using in-situ Raman spectroscopy and hydrogen-deuterium isotopic exchange. The dynamic Raman spectra revealed the decay of the ν(C-H) peak and rise of the ν(C-D) peak as isotopic exchange took place at the

α carbon of MA. A step-by-step model of keto-enol tautomerization and isotopic exchange of MA was used to simulate the decrease of the ν(C-H) peak ($I_{CH}(t)$) and to derive the enolization rate coefficient (k_1) of MA at 90% RH. The result showed a 10-fold increase of k_1 compared to the bulk measurements[22] in the smallest droplets, with a factor 8 in larger droplets. In addition, a pseudo-first order approximation was adopted to perform quantitative analysis of size- and RH-dependence of keto-enol tautomerization of MA. Our results are consistent with slower reaction rates in drier conditions owing to the slower diffusion rate of water and gas-droplet exchange that led to accumulation of HOD in the droplet, eventually promoting the reverse isotopic exchange (D→H). The size of the droplets was found to be another factor that governed the rate of tautomerization as the gas-droplet exchange rate depends on surface to volume ratio. To the best of our knowledge, accelerated keto-enol tautomerization rates of MA in aerosol has not been previously reported, and we note that these Raman spectroscopic measurements provide non-destructive measurements of enhanced reaction kinetics where gas phase reactions can be neglected. Since MA is an atmospherically relevant molecule, the findings from this work have potentially broad impacts on the current understanding of aqueous OA particles, with many aspects of the unique chemistry requiring further investigation.

Associated Content

Supporting Information

Mie scattering images of MA droplets, Calculated WSR versus RH data, Refractive indices used in each RH condition, simulated $I_{CH}(t)$ and $I_{CD}(t)$ fit for MA droplets of all sizes at 90% RH, and mathematical description of step-by-step model for keto-enol tautomerization of MA coupled with isotopic exchange reactions.

Acknowledgement

This work was supported by the NSF through the NSF Center for Aerosol Impacts on Chemistry of the Environment (CAICE), CHE-1801971. We thank Joseph Taulane for his contributions to the project. All relevant data will be made available online at the CAICE UC San Diego Library Digital Collections (https://doi.org/10.6075/J0DZ06T2).

ToC Image

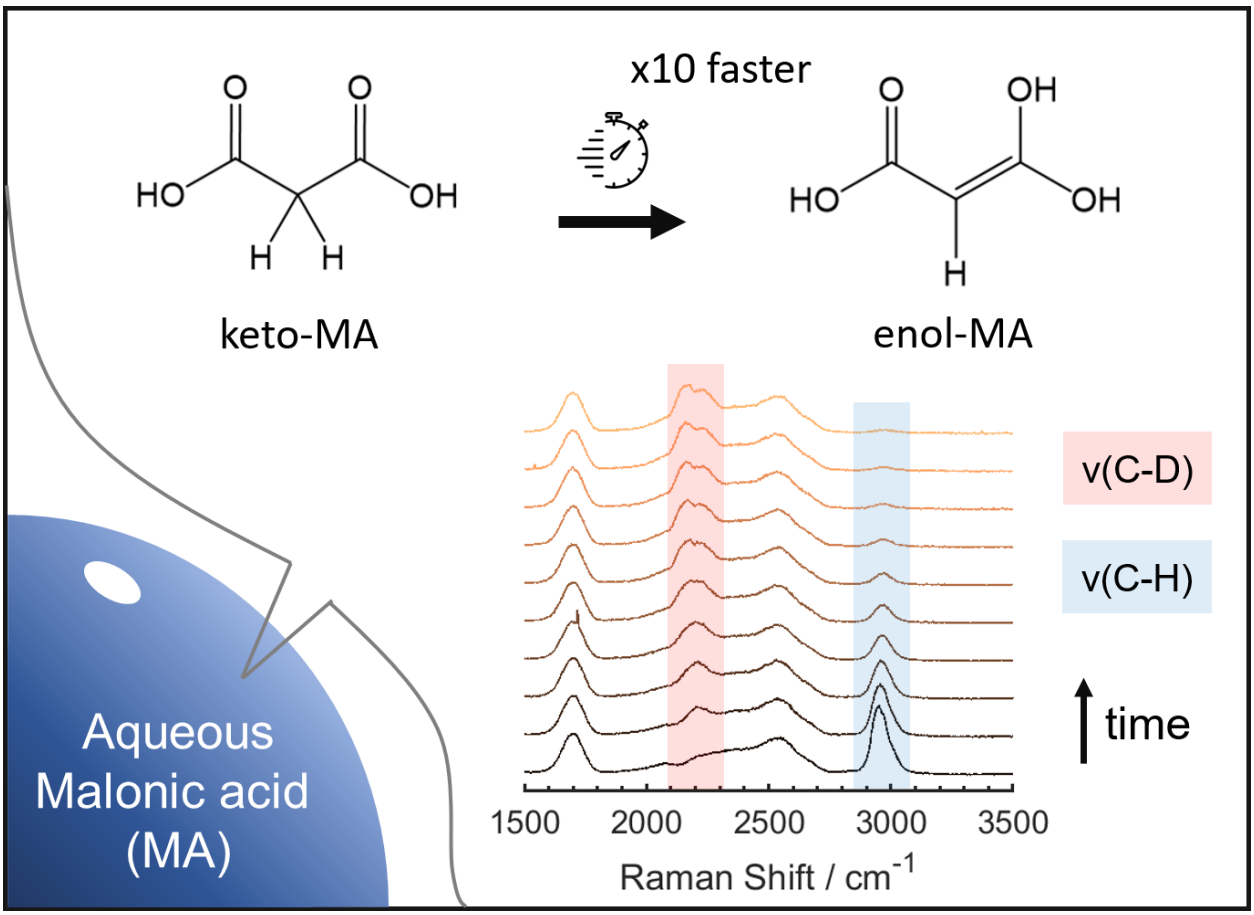
x10 faster
keto-MA
enol-MA
Aqueous
Malonic acid
(MA)
v(C-D)
v(C-H)
time
1500
2000
2500
3000
3500
Raman Shift / cm-1

References

(1) McCormick, R. A.; Ludwig, J. H. Climate Modification by Atmospheric Aerosols. *Science (80-.).* **1967**, *156* (3780), 1358 LP – 1359.

(2) IPCC. *Climate Change 2014 Part A: Global and Sectoral Aspects*; 2014.

(3) Mauderly, J. L.; Chow, J. C. *Health Effects of Organic Aerosols*; 2008; Vol. 20.

(4) Li, Y.; Shiraiwa, M. Timescales of Secondary Organic Aerosols to Reach Equilibrium at Various Temperatures and Relative Humidities. *Atmos. Chem. Phys.* **2019**, *19* (9), 5959–5971.

(5) Shiraiwa, M.; Seinfeld, J. H. Equilibration Timescale of Atmospheric Secondary Organic Aerosol Partitioning. *Geophys. Res. Lett.* **2012**, *39* (24), L24801.

(6) Chan, M. N.; Zhang, H.; Goldstein, A. H.; Wilson, K. R. Role of Water and Phase in the Heterogeneous Oxidation of Solid and Aqueous Succinic Acid Aerosol by Hydroxyl Radicals. *J. Phys. Chem. C* **2014**, *118* (50), 28978–28992.

(7) Gentner, D. R.; Jathar, S. H.; Gordon, T. D.; Bahreini, R.; Day, D. A.; El Haddad, I.; Hayes, P. L.; Pieber, S. M.; Platt, S. M.; De Gouw, J.; Goldstein, A. H.; Harley, R. A.; Jimenez, J. L.; Prévôt, A. S. H.; Robinson, A. L. Review of Urban Secondary Organic Aerosol Formation from Gasoline and Diesel Motor Vehicle Emissions. *Environ. Sci. Technol.* **2017**, *51* (3), 1074–1093.

(8) Volkamer, R.; Jimenez, J. L.; San Martini, F.; Dzepina, K.; Zhang, Q.; Salcedo, D.; Molina, L. T.; Worsnop, D. R.; Molina, M. J. Secondary Organic Aerosol Formation from Anthropogenic Air Pollution: Rapid and Higher than Expected. *Geophys. Res. Lett.* **2006**, *33* (17), 7–10.

(9) Shrivastava, M.; Cappa, C. D.; Fan, J.; Goldstein, A. H.; Guenther, A. B.; Jimenez, J. L.; Kuang, C.; Laskin, A.; Martin, S. T.; Ng, N. L.; Petaja, T.; Pierce, J. R.; Rasch, P. J.; Roldin, P.; Seinfeld, J. H.; Shilling, J.; Smith, J. N.; Thornton, J. A.; Volkamer, R.; Wang, J.; Worsnop, D. R.; Zaveri, R. A.; Zelenyuk, A.; Zhang, Q. Recent Advances in Understanding Secondary Organic Aerosol:

Implications for Global Climate Forcing. *Rev. Geophys.* **2017**, *55* (2), 509–559.

(10) Liu, M. J.; Wiegel, A. A.; Wilson, K. R.; Houle, F. A. Aerosol Fragmentation Driven by Coupling of Acid-Base and Free-Radical Chemistry in the Heterogeneous Oxidation of Aqueous Citric Acid by OH Radicals. *J. Phys. Chem. A* **2017**, *121* (31), 5856–5870.

(11) Banerjee, S.; Gnanamani, E.; Yan, X.; Zare, R. N. Can All Bulk-Phase Reactions Be Accelerated in Microdroplets? *Analyst* **2017**, *142* (9), 1399–1402.

(12) Crawford, E. A.; Esen, C.; Volmer, D. A. Real Time Monitoring of Containerless Microreactions in Acoustically Levitated Droplets via Ambient Ionization Mass Spectrometry. *Anal. Chem.* **2016**, *88* (17), 8396–8403.

(13) Yan, X.; Bain, R. M.; Cooks, R. G. Organic Reactions in Microdroplets: Reaction Acceleration Revealed by Mass Spectrometry. *Angew. Chemie - Int. Ed.* **2016**, *55* (42), 12960–12972.

(14) Li, Y.; Liu, Y.; Gao, H.; Helmy, R.; Wuelfing, W. P.; Welch, C. J.; Cooks, R. G. Accelerated Forced Degradation of Pharmaceuticals in Levitated Microdroplet Reactors. *Chem. - A Eur. J.* **2018**, *24* (29), 7349–7353.

(15) Wei, Z.; Li, Y.; Cooks, R. G.; Yan, X. Accelerated Reaction Kinetics in Microdroplets: Overview and Recent Developments. *Annu. Rev. Phys. Chem.* **2020**, *71*, 31–51.

(16) Kawamura, K.; Usukura, K. Distributions of Low Molecular Weight Dicarboxylic Acids in the North Pacific Aerosol Samples. *J. Oceanogr.* **1993**, *49* (3), 271–283.

(17) Leopold, K. R.; Haim, A. Equilibrium, Kinetics, and Mechanism of the Malonic Acid–Iodine Reaction. *Int. J. Chem. Kinet.* **1977**, *9* (1), 83–95.

(18) Ghorai, S.; Laskin, A.; Tivanski, A. V. Spectroscopic Evidence of Keto Enol Tautomerism in

Deliquesced Malonic Acid Particles. *J. Phys. Chem. A* **2011**, *115* (17), 4373–4380.

(19) Yamabe, S.; Tsuchida, N.; Miyajima, K. Reaction Paths of Keto-Enol Tautomerization of β-Diketones. *J. Phys. Chem. A* **2004**, *108* (14), 2750–2757.

(20) Jansson, E. T.; Lai, Y. H.; Santiago, J. G.; Zare, R. N. Rapid Hydrogen-Deuterium Exchange in Liquid Droplets. *J. Am. Chem. Soc.* **2017**, *139* (20), 6851–6854.

(21) Rovelli, G.; Jacobs, M. I.; Willis, M. D.; Rapf, R. J.; Prophet, A. M.; Wilson, K. R. A Critical Analysis of Electrospray Techniques for the Determination of Accelerated Rates and Mechanisms of Chemical Reactions in Droplets. *Chem. Sci.* **2020**, *11* (48), 13026–13043.

(22) Hansen, E. W.; Ruoff, P. Estimation of Malonic Acid and Methylmalonic Acid Enolization Rate Constants by an Isotopic-Exchange Reaction Using 1H NMR Spectroscopy. *J. Phys. Chem.* **1988**, *92* (9), 2641–2645.

(23) Lee, C. R.; Kim, H. S.; Jang, I. H.; Im, J. H.; Park, N. G. Pseudo First-Order Adsorption Kinetics of N719 Dye on TiO2 Surface. *ACS Appl. Mater. Interfaces* **2011**, *3* (6), 1953–1957.

(24) Anzo, K.; Harada, M.; Okada, T. Enhanced Kinetics of Pseudo First-Order Hydrolysis in Liquid Phase Coexistent with Ice. *J. Phys. Chem. A* **2013**, *117* (41), 10619–10625.

(25) Bockisch, C.; Lorance, E. D.; Hartnett, H. E.; Shock, E. L.; Gould, I. R. Kinetics and Mechanisms of Dehydration of Secondary Alcohols under Hydrothermal Conditions. *ACS Earth Sp. Chem.* **2018**, *2* (8), 821–832.

(26) Nadler, K. A.; Kim, P.; Huang, D. L.; Xiong, W.; Continetti, R. E. Water Diffusion Measurements of Single Charged Aerosols Using H2O/D2O Isotope Exchange and Raman Spectroscopy in an Electrodynamic Balance. *Phys. Chem. Chem. Phys.* **2019**, *21* (27), 15062–15071.

(27) Kim, P.; Xiong, W.; Continetti, R. E. Evolution of Hydrogen-Bond Interactions within Single Levitated Metastable Aerosols Studied by in Situ Raman Spectroscopy. *J. Phys. Chem. B* **2020**, *124* (42), 9385–9395.

(28) Trevitt, A. J.; Wearne, P. J.; Bieske, E. J. Calibration of a Quadrupole Ion Trap for Particle Mass Spectrometry. *Int. J. Mass Spectrom.* **2007**, *262* (3), 241–246.

(29) Glantschnig, W. J.; Chen, S.-H. Light Scattering from Water Droplets in the Geometrical Optics Approximation. *Appl. Opt.* **1981**, *20* (14), 2499.

(30) Graßmann, A.; Peters, F. Size Measurement of Very Small Spherical Particles by Mie Scattering Imaging (MSI). *Part. Part. Syst. Charact.* **2004**, *21* (5), 379–389.

(31) Cai, C.; Miles, R. E. H.; Cotterell, M. I.; Marsh, A.; Rovelli, G.; Rickards, A. M. J.; Zhang, Y. H.; Reid, J. P. Comparison of Methods for Predicting the Compositional Dependence of the Density and Refractive Index of Organic-Aqueous Aerosols. *J. Phys. Chem. A* **2016**, *120* (33), 6604–6617.

(32) Salomon, M. *Thermodynamic Properties of Liquid H2O and D2O and Their Mixtures*; United States. National Aeronautics and Space Administration. “NASA Technical Note.” Print.: Washington, D.C., 1969.

(33) Bykov, S. V.; Myshakina, N. S.; Asher, S. A. Dependence of Glycine CH2 Stretching Frequencies on Conformation, Ionization State, and Hydrogen Bonding. *J. Phys. Chem. B* **2008**, *112* (18), 5803–5812.

(34) Zhou, S.; Shiraiwa, M.; McWhinney, R. D.; Pöschl, U.; Abbatt, J. P. D. Kinetic Limitations in Gas-Particle Reactions Arising from Slow Diffusion in Secondary Organic Aerosol. *Faraday Discuss.* **2013**, *165*, 391–406.

(35) Slade, J. H.; Knopf, D. A. Multiphase OH Oxidation Kinetics of Organic Aerosol: The Role of Particle

Phase State and Relative Humidity. *Geophys. Res. Lett.* **2014**, *41* (14), 5297–5306.

(36) Chang, P.; Chen, Z.; Zhang, Y.; Liu, Y. Direct Measurement of Aerosol PH in Individual Malonic Acid and Citric Acid Droplets under Different Relative Humidity Conditions via Raman Spectroscopy. *Chemosphere* **2020**, *241*, 124960.

(37) Seinfeld, J. H.; Pandis, S. N. *Atmospheric Chemistry and Physics: From Air Pollution to Climate Change*; John Wiley & Sons, 2016.

(38) Peng, C.; Chan, C. K.; Chow, A. H. L. Hygroscopic Study of Glucose, Citric Acid, and Sorbitol Using an Electrodynamic Balance: Comparison with UNIFAC Predictions. *Aerosol Sci. Technol.* **2001**, *35* (3), 753–758.

(39) Wilson, K. R.; Prophet, A. M.; Rovelli, G.; Willis, M. D.; Rapf, R. J.; Jacobs, M. I. A Kinetic Description of How Interfaces Accelerate Reactions in Micro-Compartments. *Chem. Sci.* **2020**, *11* (32), 8533–8545.

(40) Hua, W.; Chen, X.; Allen, H. C. Phase-Sensitive Sum Frequency Revealing Accommodation of Bicarbonate Ions, and Charge Separation of Sodium and Carbonate Ions within the Air/Water Interface. *J. Phys. Chem. A* **2011**, *115* (23), 6233–6238.

(41) Blower, P. G.; Shamay, E.; Kringle, L.; Ota, S. T.; Richmond, G. L. Surface Behavior of Malonic Acid Adsorption at the Air/Water Interface. *J. Phys. Chem. A* **2013**, *117* (12), 2529–2542.

(42) Liu, D.; Ma, G.; Levering, L. M.; Allen, H. C. Vibrational Spectroscopy of Aqueous Sodium Halide Solutions and Air−Liquid Interfaces: Observation of Increased Interfacial Depth. *J. Phys. Chem. B* **2004**, *108* (7), 2252–2260.

(43) Shrestha, M.; Luo, M.; Li, Y.; Xiang, B.; Xiong, W.; Grassian, V. H. Let There Be Light: Stability of Palmitic Acid Monolayers at the Air/Salt Water Interface in the Presence and Absence of

Simulated Solar Light and a Photosensitizer. *Chem. Sci.* **2018**, *9* (26), 5716–5723.

(44) J. R. Keeffe, A. J. Kresge, and N. P. S. Generation of Simple Enols by Photooxidation. Keto-Enol Equilibrium Constants of Some Aliphatic Systems in Aqueous Solution. *J. Am. Chem. Soc.* **1988**, *110*, 1993–1995.

(45) Lim, Y. B.; Tan, Y.; Perri, M. J.; Seitzinger, S. P.; Turpin, B. J. Aqueous Chemistry and Its Role in Secondary Organic Aerosol (SOA) Formation. *Atmos. Chem. Phys.* **2010**, *10* (21), 10521–10539.

(46) Lei, X.; Wang, W.; Cai, J.; Wang, C.; Liu, F.; Wang, W. Atmospheric Chemistry of Enols: Vinyl Alcohol + OH + O 2 Reaction Revisited. *J. Phys. Chem. A* **2019**, *123* (14), 3205–3213.

(47) Narukawa, M.; Kawamura, K.; Li, S. M.; Bottenheim, J. W. Dicarboxylic Acids in the Arctic Aerosols and Snowpacks Collected during ALERT 2000. *Atmos. Environ.* **2002**, *36* (15–16), 2491–2499.

(48) Zuend, A.; Marcolli, C.; Booth, A. M.; Lienhard, D. M.; Soonsin, V.; Krieger, U. K.; Topping, D. O.; McFiggans, G.; Peter, T.; Seinfeld, J. H. New and Extended Parameterization of the Thermodynamic Model AIOMFAC: Calculation of Activity Coefficients for Organic-Inorganic Mixtures Containing Carboxyl, Hydroxyl, Carbonyl, Ether, Ester, Alkenyl, Alkyl, and Aromatic Functional Groups. *Atmos. Chem. Phys.* **2011**, *11* (17), 9155–9206.

(49) Peng, C.; Chan, M. N.; Chan, C. K. The Hygroscopic Properties of Dicarboxylic and Multifunctional Acids: Measurements and UNIFAC Predictions. *Environ. Sci. Technol.* **2001**, *35* (22), 4495–4501.